Separation Science and Technology
Publication details, including instructions for authors and subscription information:
http://www.informaworld.com/smpp/title~content=t713708471

Theoretical Analysis of the Effect of Membrane Morphology on Fouling during Microfiltration

Chia-Chi Ho[a]; Andrew L. Zydney[a]
[a] DEPARTMENT OF CHEMICAL ENGINEERING, UNIVERSITY OF DELAWARE, NEWARK, DELAWARE, USA

Online publication date: 15 September 1999

To cite this Article Ho, Chia-Chi and Zydney, Andrew L.(1999) 'Theoretical Analysis of the Effect of Membrane Morphology on Fouling during Microfiltration', Separation Science and Technology, 34: 13, 2461 — 2483
To link to this Article: DOI: 10.1081/SS-100100785
URL: http://dx.doi.org/10.1081/SS-100100785

SEPARATION SCIENCE AND TECHNOLOGY, **34**(13), pp. 2461–2483, 1999

Theoretical Analysis of the Effect of Membrane Morphology on Fouling during Microfiltration

CHIA-CHI HO and ANDREW L. ZYDNEY*
DEPARTMENT OF CHEMICAL ENGINEERING
UNIVERSITY OF DELAWARE
NEWARK, DELAWARE 19716, USA

ABSTRACT

Previous studies of membrane fouling have often employed one of the classical blocking laws to describe the variation of filtrate flux with time. However, these models implicitly assume that the membrane has straight-through noninterconnected pores, even though most commercial microfiltration and ultrafiltration membranes have a highly interconnected pore structure. We have developed a theoretical model for the effects of pore blockage on the fluid velocity and pressure profiles within membranes having different interconnected pore structures assuming Darcy flow in the porous membrane. Model calculations are in good agreement with filtrate flux data obtained during protein microfiltration using membranes with very different pore morphologies. The results clearly demonstrate that the membrane pore connectivity has a significant influence on the flux decline due to the possibility for fluid to flow around the pore blockage, an effect which has been ignored in previous studies.

Key Words. Microfiltration; Fouling; Membrane morphology

INTRODUCTION

Experimental data for membrane fouling are often analyzed using either cake filtration theory (1) or one of the classical "blocking laws" initially developed for particle filtration. The blocking laws were first introduced by Hermans and Bredée (2, 3) in their analysis of filtrate flux data obtained during filtration of dilute particle suspensions through filter cloths, cotton sheets, and

* To whom correspondence should be addressed. Telephone: 302-831-2399. FAX: 302-831-1048. E-mail: zydney@che.udel.edu

layers of filter aid. The complete blocking law was developed by assuming that "the filtering medium may be regarded as a collection of parallel capillary tubes of constant diameter and length which become blocked in such a way that every time a particle passes into a tube that the latter is completely sealed" (3). The standard blocking law was also developed assuming that the membrane consisted of an array of parallel capillaries but with the fouling occurring "in such a way that the inside volume of the tubes decreases proportionally to the volume of filtrate passed through" the membrane (3).

Hermans and Bredée (2, 3), Gonsalves (4), and Grace (5) showed that the total filtrate volume (V) versus filtration time (t) predicted by the cake filtration and blocking laws could all be written in a common mathematical form as

$$\frac{d^2t}{dV^2} = k\left(\frac{dt}{dV}\right)^n \tag{1}$$

The exponent n characterizes the filtration model, with $n = 0$ for cake filtration, $n = \frac{3}{2}$ for standard blocking, and $n = 2$ for complete blocking. Hermans and Bredée (3) also coined the term "intermediate blocking" to describe the filtration behavior with $n = 1$, although no physical interpretation of this situation was provided. Hermia (6) subsequently showed that the intermediate blocking law could be derived from the complete blocking model by assuming that the deposited particles could settle on top of other particles on the filter surface.

The different blocking laws have been used for over 50 years to analyze and interpret filtrate flux data. There has been considerable recent interest in the application of these models to protein microfiltration (7–11), with the fouling attributed to the physical deposition of large protein aggregates on or within the membrane pore structure (12). However, these models have often been applied to the fouling of polymeric microfiltration membranes having highly interconnected pore structures, e.g., polyethersulfone (7), polyvinylidene fluoride (8, 9, 11), and mixed cellulose ester (9) membranes. Thus, the underlying assumption in the blocking laws that the membrane consists of an array of parallel capillary tubes is clearly invalid. In particular, particle (or aggregate) deposition on the upper surface of these microfiltration membranes would not be able to completely seal off or block that fraction of the membrane area since the interconnected pore structure would allow the fluid to flow around and under the "blockage" as it percolates through the membrane. Ho and Zydney (13) recently showed that membranes having an interconnected pore structure do foul much more slowly than membranes with straight-through (nonconnected) pores, with the data suggesting that aggregate deposition only disturbs the filtrate flow over a small penetration distance into the interconnected pore structure of these membranes.

The objective of this study was to develop a mathematical description of the filtrate flow through membranes having interconnected pore structures which

can be used to analyze and interpret filtrate flux data obtained during protein microfiltration. The velocity profiles within the porous membrane were described using Darcy's law, with different Darcy permeabilities used in the directions normal to and parallel to the membrane surface for membranes with different degrees of pore connectivity. Model calculations were then compared with experimental data for protein fouling obtained with microfiltration membranes having different pore structures.

THEORY

In order to account for the effects of pore connectivity on the filtrate flux, we need to specifically evaluate the changes in flow distribution within the membrane as the upper surface becomes fouled. We assume that the initial deposition of particles/colloids occurs uniformly and randomly over the membrane surface, with the upper surface of the partially fouled membrane shown schematically in the upper panel of Fig. 1. At low surface coverage the flow through this partially fouled membrane can be described by a Krogh-cylinder-type model used previously to analyze flow in capillary beds (14) and hollow fiber membrane bioreactors (15). Thus, we consider the flow through a single cylindrical region of the membrane with a blockage located at the center (lower left panel of Fig. 1). The radius of this cylinder is directly related to the fraction of the membrane surface that is blocked (covered) at time t, i.e., $f = (r_{\text{blockage}}/r_{\text{cylinder}})^2$. As the membrane becomes more highly fouled, the fluid flow will occur primarily through the gaps (or holes) between protein aggregates in the fouling layer, leading to the physical model shown in the lower right panel. In this case the blockage covers an annular region with the fractional surface coverage given as $f = 1 - (r_{\text{open}}/r_{\text{cylinder}})^2$.

The velocity profiles within the porous membrane are assumed to be given by Darcy's law:

$$V_{\text{r}} = -K_{\text{r}} \frac{\partial P}{\partial r}; \qquad V_{\text{z}} = -K_{\text{z}} \frac{\partial P}{\partial z} \tag{2}$$

where K_{r} and K_{z} are the Darcy permeabilities in the radial and transverse directions, respectively. Thus, a membrane with straight-through pores would have $K_{\text{r}} = 0$ (no radial flow), while a truly isotropic membrane would have $K_{\text{r}} = K_{\text{z}}$. The velocities V_{r} and V_{z} must satisfy the continuity equation, which for an incompressible fluid is

$$\nabla \cdot V = \frac{1}{r} \frac{\partial}{\partial r} (rV_{\text{r}}) + \frac{\partial V_{\text{z}}}{\partial z} = 0 \tag{3}$$

Substitution of Eq. (2) into Eq. (3) yields a second-order partial differential

MARCEL DEKKER, INC.
270 Madison Avenue, New York, New York 10016

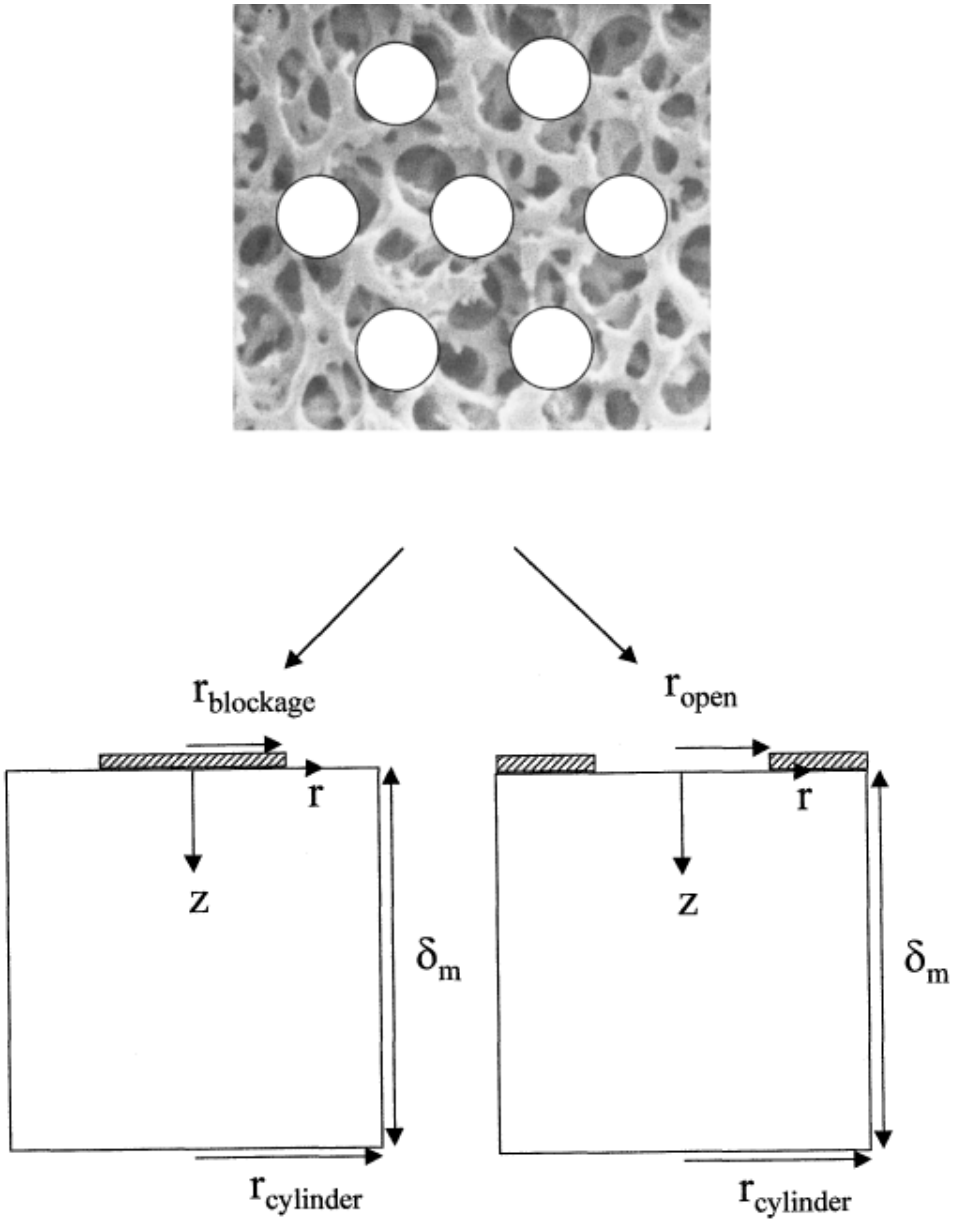

FIG. 1 Schematic of the top surface of a partially fouled membrane showing the Krogh cylinder approximation with central blockage (left panel) or central void (right panel).

equation for the local pressure which is in the form of Laplace's equation:

$$\frac{K_r}{r}\frac{\partial}{\partial r}\left(r\frac{\partial P}{\partial r}\right) + K_z\frac{\partial^2 P}{\partial z^2} = 0 \qquad (4)$$

A symmetry condition is applied at the axis of the cylinder:

$$r = 0; \qquad \partial P/\partial r = 0 \qquad (5)$$

MARCEL DEKKER, INC.
270 Madison Avenue, New York, New York 10016

and a no flux ($V_r = 0$) condition is applied at the outer boundary:

$$r = r_{\text{cylinder}}; \qquad \partial P/\partial r = 0 \tag{6}$$

where Eq. (6) is developed from the requirement that the flow in each cylindrical region is self-contained. The pressure at the downstream (filtrate) surface of the membrane is assumed to be uniform:

$$z = \delta_m; \qquad P = P_{\text{filtrate}} \tag{7}$$

The boundary condition at the upstream (feed) surface must account for the effects of pore blockage. In order to develop a more general model, we allow for the possibility that the fouling layer (blockage) is partially permeable to the fluid with hydraulic permeability L_p. The permeability of this blockage is assumed to be constant (independent of position and extent of fouling). This assumption should be valid for isolated particulate foulants, although it will not be applicable for systems in which additional foulant can chemically attach to the deposit or form a multilayer particulate cake. This leads to a split boundary condition at $z = 0$, with the form of the boundary condition dependent on the physical picture of the fouling layer. For the situation shown in the lower left panel of Fig. 1 we have

$$z = 0; \qquad L_p(P_{\text{feed}} - P) = V_z = -K_z \frac{\partial P}{\partial z} \qquad 0 \le r \le r_{\text{blockage}} \tag{8a}$$

$$z = 0; \qquad P = P_{\text{feed}} \qquad r_{\text{blockage}} < r \le r_{\text{cylinder}} \tag{8b}$$

while for the situation shown in the lower right panel the condition at $z = 0$ is

$$z = 0; \qquad P = P_{\text{feed}} \qquad 0 \le r \le r_{\text{open}} \tag{9a}$$

$$z = 0; \qquad L_p(P_{\text{feed}} - P) = V_z = -K_z \frac{\partial P}{\partial z} \qquad r_{\text{open}} < r \le r_{\text{cylinder}} \tag{9b}$$

In both cases, P_{feed} is a constant, independent of the flow rate, since the Reynolds numbers in this system are all small. Note that if the blocked pores are completely impermeable to flow ($L_p = 0$), Eqs. (8a) and (9b) reduce to $\partial P/\partial z = 0$ over that region of the membrane. Equations (4)–(8) can be nondimensionalized using the membrane thickness (δ_m) and the radius of the pore blockage (r_{blockage}) as the characteristic dimensions yielding

$$\frac{1}{\rho}\frac{\partial}{\partial \rho}\left(\rho \frac{\partial \theta}{\partial \rho}\right) + K\frac{\partial^2 \theta}{\partial Y^2} = 0 \tag{10}$$

where $\theta = [(P - P_{\text{feed}})/(P_{\text{filtrate}} - P_{\text{feed}})]$, $\rho = r/r_{\text{blockage}}$, and $Y = z/\delta_m$. A similar nondimensionalization can be used with Eq. (9) but with r_{open} replacing

MARCEL DEKKER, INC.
270 Madison Avenue, New York, New York 10016

$r_{blockage}$. Equation (10) is expressed in terms of the nondimensional permeability ratio

$$K = \frac{K_z}{K_r}\left(\frac{r_{blockage}}{\delta_m}\right)^2 \tag{11}$$

The boundary conditions at the upstream surface of the membrane (Eqs. 8a and 8b) become

$$Y = 0; \qquad \partial\theta/\partial Y = \beta\theta \qquad 0 \le \rho \le 1 \tag{12a}$$

$$Y = 0; \qquad \theta = 0 \qquad 1 < \rho \le f^{-1/2} \tag{12b}$$

where $\beta = \delta_m L_p/K_z$ is the dimensionless permeability of the fouling deposit and $f = (r_{blockage}/r_{cylinder})^2$ is the fractional surface coverage. The dimensionless form of Eq. (9) is analogous to Eq. (12) with the outer boundary now at $(1 - f)^{-1/2}$. The fluid flow and pressure profiles are thus completely determined by three dimensionless parameters: f, which is related to the extent of fouling; β, which is related to the permeability of the fouling layer; and K, which describes the relative permeability of the porous membrane in the axial and radial directions and is thus a function of the pore connectivity as well as the membrane thickness.

Equation (10) was solved numerically using a finite difference representation accurate to $O(\Delta\rho^2)$ and $O(\Delta Y^2)$. In order to concentrate grid points in the region of steepest pressure gradient, the variable transformation

$$X = 1 - \frac{1}{A}\ln[\rho(1 - e^A) + e^A] \tag{13}$$

was used in the radial direction with A an adjustable parameter which controls the details of the grid spacing. The difference equations were solved using the DLSLXG subroutine in the IMSL math library using 100 grid points in both the radial and axial directions with $A = 5$ in the radial transformation. Numerical convergence was verified by repeating the calculations using twice as many grid points in both directions. Calculations were conducted on an IBM PC requiring approximately 5 minutes. The dimensionless filtrate flux through the membrane was then evaluated from the dimensionless pressure as

$$\frac{J}{J_0} = \int^{f^{-1/2}} \left.\frac{\partial\theta}{\partial Y}\right|_{Y=1} 2\rho d\rho \tag{14}$$

where J_0 is the flux through the clean (nonfouled) membrane. The upper limit on the integral in Eq. (14) was $(1 - f)^{-1/2}$ for calculations performed with the annular blockage (Eq. 9).

THEORETICAL RESULTS

Figure 2 shows the effects of the radial permeability (K_r) on the predicted pressure profiles and flow streamlines for a partially fouled membrane

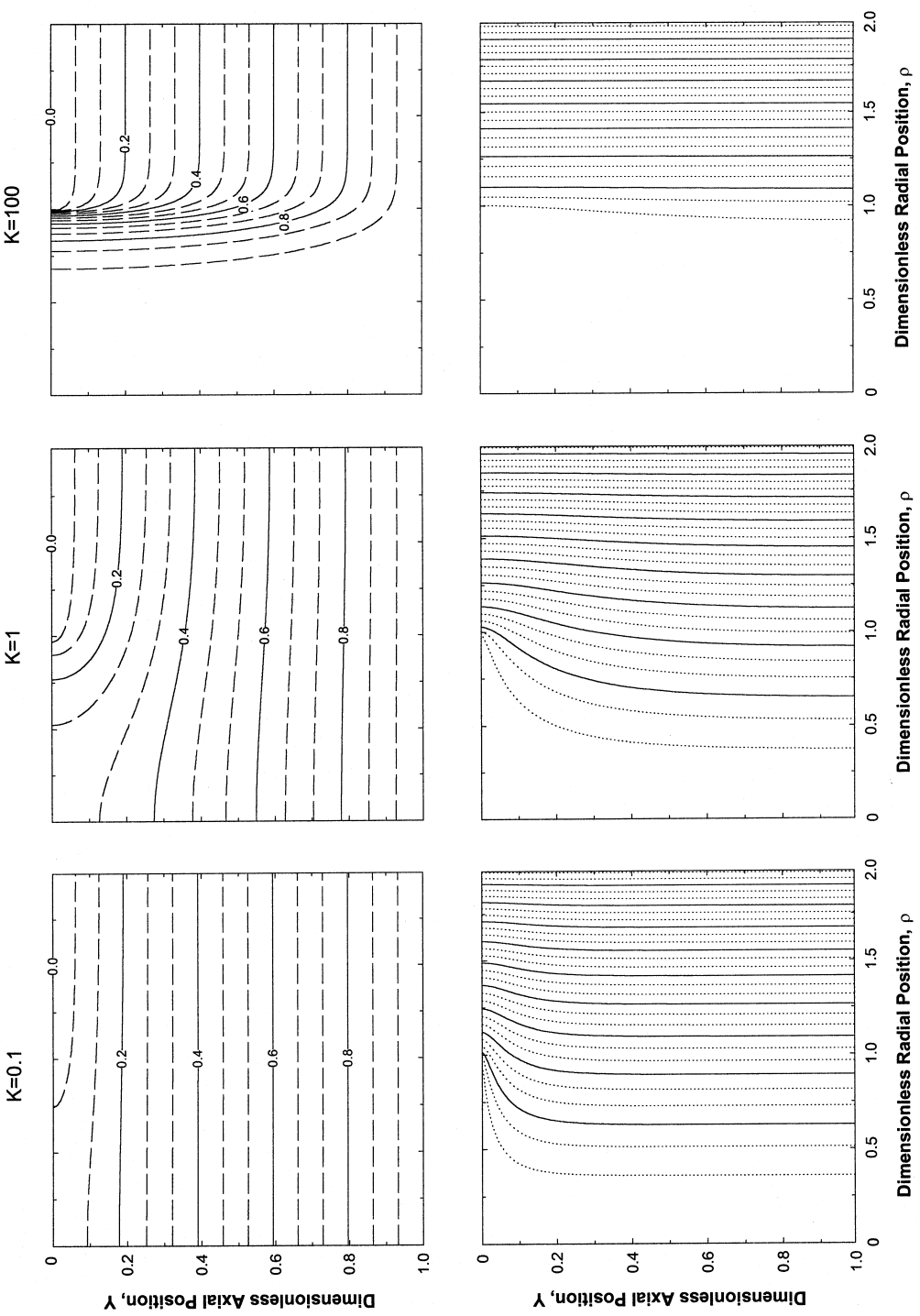

FIG. 2 Pressure profiles and streamlines within the membrane for $r_{blockage}/r_{cylinder} = 0.5$ and $\beta = 0$ for $K = 0.1$, $K = 1$, and $K = 100$.

MARCEL DEKKER, INC.
270 Madison Avenue, New York, New York 10016

($f = 0.25$) assuming a completely impermeable fouling layer ($\beta = 0$) using the configuration shown in the lower left panel of Fig. 1. In each case the streamlines were calculated directly from the velocities as

$$\psi = \int r(V_z dr - V_r dz) \tag{15}$$

with V_z and V_r evaluated by numerical differentiation of the pressure using the Darcy flow equations (Eq. 2). Results are shown for three values of the permeability ratio: $K = 0.1$, 1, and 100. At large K the fluid flow occurs almost entirely through the region outside of the pore blockage ($\rho > 1$), with the pressure in the cylindrical region beneath the blockage remaining close to $\theta = 1$ (i.e., $P = P_{\text{filtrate}}$) at all axial positions. This causes a steep radial pressure gradient at $\rho = 1$; however, the radial velocity remains small since $K_r < K_z$. As the permeability ratio decreases, the radial pressure gradient causes the fluid to flow around and under the pore blockage. When $K = 0.1$ this radial flow is sufficiently strong that the pressure profile within the membrane becomes nearly uniform for $Y > 0.15$. The pore blockage under these conditions has relatively little effect on the total flow rate through most of the membrane, with $J/J_0 = 0.97$ even though the pore blockage covers 25% of the upper surface area of the membrane. Similar behavior was seen with the centrally located void, with the fluid flow moving radially outward and under the annular blockage.

The effects of pore blockage on the normalized flux (J/J_0) are shown explicitly in Fig. 3. The results are plotted as a function of the fractional surface coverage (f) for different values of K, with $\beta = 0$ for flow around a centrally located blockage (top panel) and for flow through a centrally located void (bottom panel). At large values of K the membrane behaves as if it has straight-through noninterconnected pores, with the normalized flux simply equal to the fractional available surface area ($1 - f$). As K decreases, the radial pressure gradient drives the fluid radially so that it passes under the pore blockage, thus reducing the effect of the blockage on the overall resistance to flow. The net result is that the normalized flux increases with decreasing K, with J/J_0 at $f = 0.9$ increasing from 0.1 when $K = 10^3$ to 0.75 (centered void) and 0.82 (centered blockage) when $K = 10^{-1}$. Interestingly, the normalized flux (J/J_0) for a given K is greater for the centered void model (bottom panel) than for the centered blockage (top panel) at small surface coverage with the reverse behavior seen at large f. At high surface coverage, where most of the membrane area is covered/blocked, it is much easier for the flow to move radially inward and under the centered blockage than it is to move radially outward from the centered void due to the increase in area with increasing radial position. However, at small surface coverage the dominant effect is the much greater radial distance covered by the fouling layer in the centered blockage model. For example,

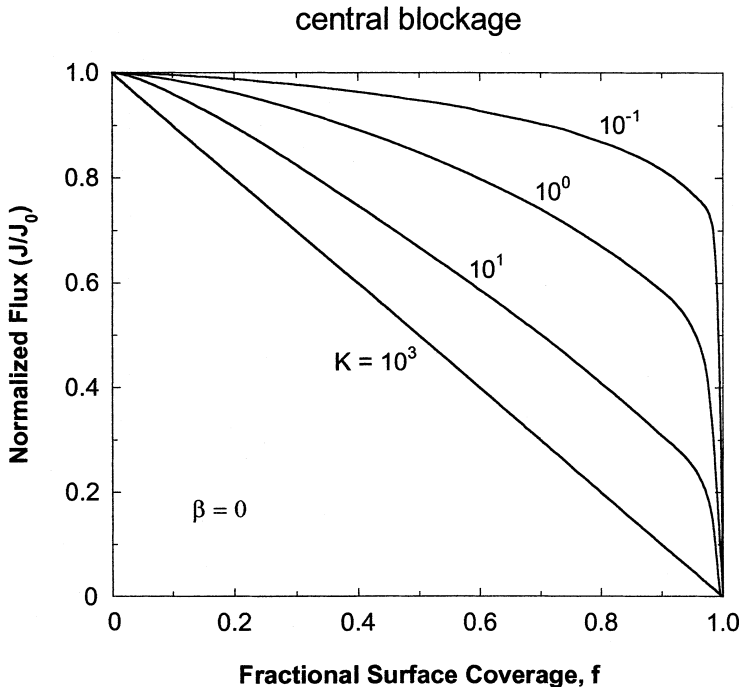

(a)

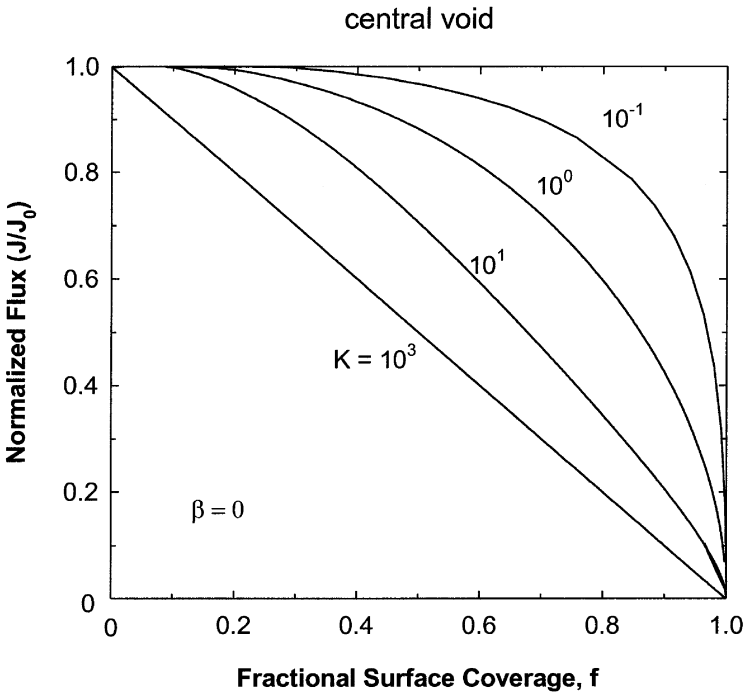

(b)

FIG. 3 Normalized filtrate flux as a function of fractional surface coverage (f) for membranes with different K values for (a) central blockage and (b) central void models.

MARCEL DEKKER, INC.
270 Madison Avenue, New York, New York 10016

when $f = 0.5$, the blockage extends out to 71% of the cylinder radius for the centered blockage model while the foulant only covers the outer 29% of the cylinder radius for the centered void model. Thus, the radial flow under the centered blockage has to travel a much greater distance under these conditions, leading to the smaller normalized flux for the centered blockage model at small surface coverage. Both blockage models predict that the majority of the flux decline for membranes with small K occurs when the last regions of the membrane become covered/blocked. This would correspond to an increase in the rate of flux decline as the membrane becomes more fouled, a phenomenon which has been observed previously in several systems (7, 9, 11).

Figure 4 shows the calculated pressure profiles and flow streamlines for a single membrane ($K = 10$) with a centered blockage ($f = 0.25$) at three different values of the dimensionless fouling layer permeability: $\beta = 0$, 0.1, and 10. When the fouling layer is highly permeable ($\beta = 10$), the flow is able to pass through the blockage relatively easily, thus the flow profile remains nearly uniform throughout the membrane. As β decreases, the disturbance in the pressure and flow profiles increases. The normalized flux also decreases with decreasing β, going from $J/J_0 = 0.98$ for $\beta = 10$ to $J/J_0 = 0.85$ for $\beta = 0$.

The effect of the different fouling layer permeabilities on the normalized flux is examined in Fig. 5 for $K = 1000$ (top panel) and $K = 0.1$ (bottom panel). The normalized flux is shown for a membrane with centered blockage for three different surface coverages: $f = 0.25$, 0.5, and 0.75. The results for zero permeability (non-permeable fouling layer) are the same as those in Fig. 3. As the fouling layer permeability increases, the normalized flux increases, with the greatest increase occurring at the highest surface coverage ($f = 0.75$). The normalized flux approaches a value of 1 as the fouling layer becomes very permeable to the fluid flow. For membranes with $K = 0.1$, the fluid is able to flow under the blockage even when the fouling layer is completely impermeable ($\beta = 0$). Thus, the normalized flux at small K is a very weak function of both the surface coverage (f) and fouling layer permeability.

MATERIALS AND METHODS

In order to verify the model predictions for the effects of pore connectivity on fouling, flux decline data were obtained with aluminum oxide (Anopore, $\delta_m = 60$ μm, Whatman, UK) and polyvinylidene fluoride membranes (PVDF, $\delta_m = 125$ μm, Millipore Corporation, Bedford, MA). The membranes were obtained from the manufacturers as 25 mm disks. The Anopore membranes have straight-through noninterconnecting pores, while the PVDF membranes have an isotropic (interconnected) pore structure as shown in the SEMs in Fig.

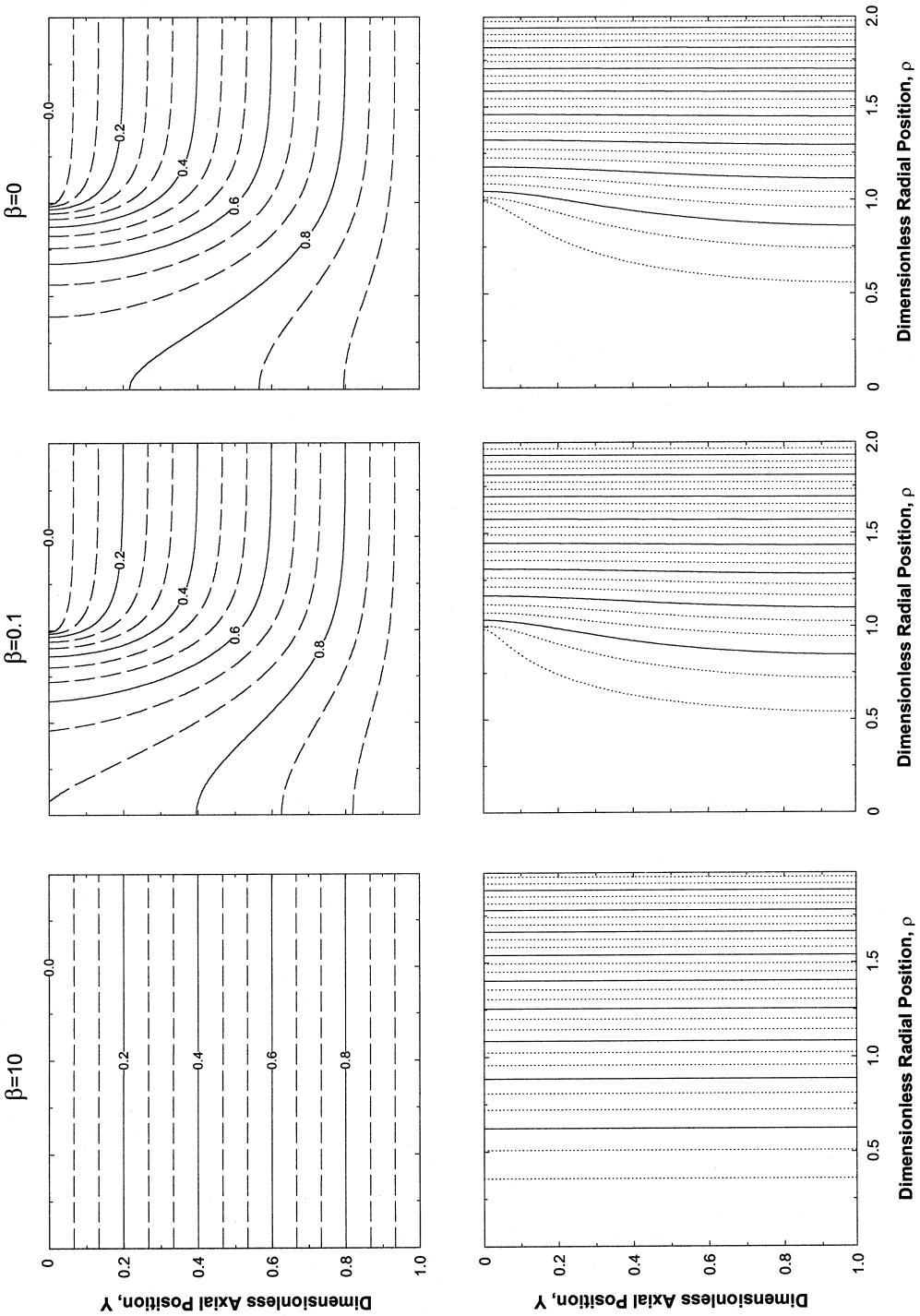

FIG. 4 Pressure profiles and streamlines within the membrane for $r_{\text{blockage}}/r_{\text{cylinder}} = 0.5$ and $K = 10$ for $\beta = 10$, $\beta = 0.1$, and $\beta = 0$.

MARCEL DEKKER, INC.
270 Madison Avenue, New York, New York 10016

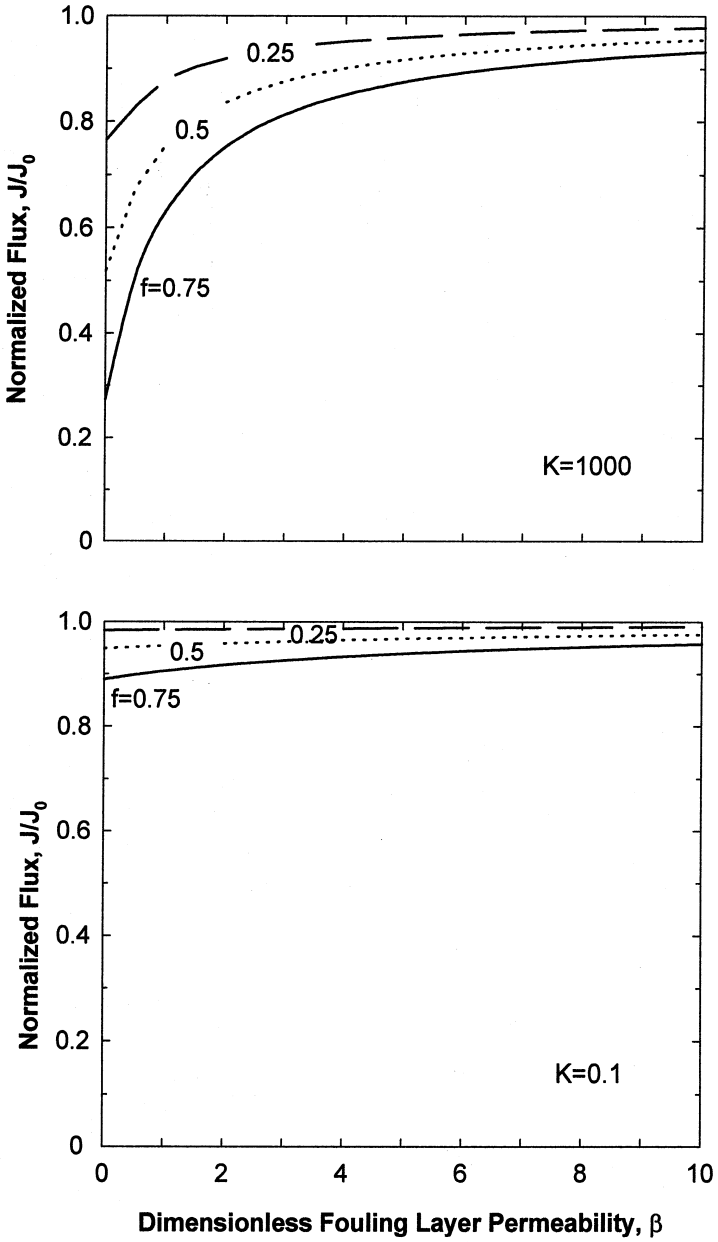

FIG. 5 Normalized filtrate flux as a function of dimensionless fouling layer permeability (β) for membranes with $K = 1000$ (top panel) and $K = 0.1$ (bottom panel).

6. Data were also obtained with two PVDF membranes in a series sandwich combination to examine the effects of membrane thickness on the flux.

Fouling experiments were performed using *S*-cysteinyl bovine serum albumin (cys-BSA) obtained from Sigma Chemical Company (catalog number A0161). Kelly and Zydney (16) showed that fouling by cys-BSA occurs entirely by the physical deposition of large protein aggregates or particles on the

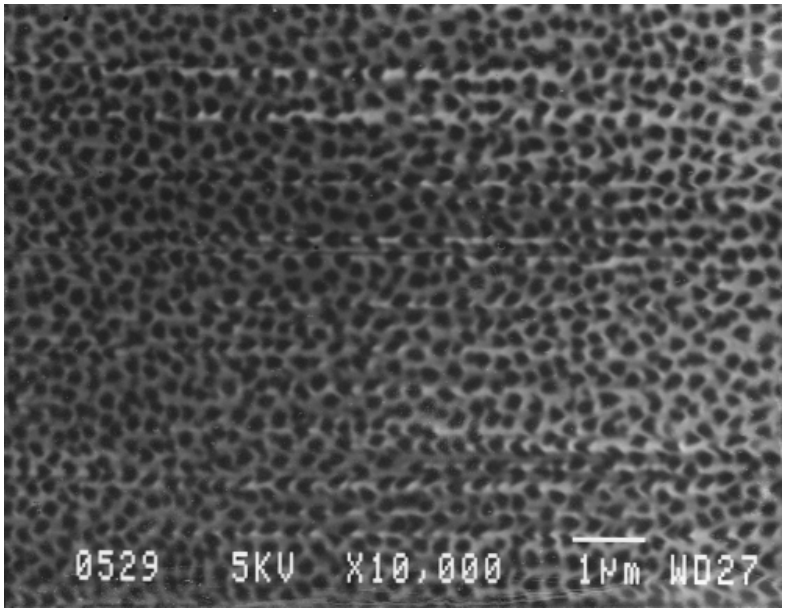

(a)

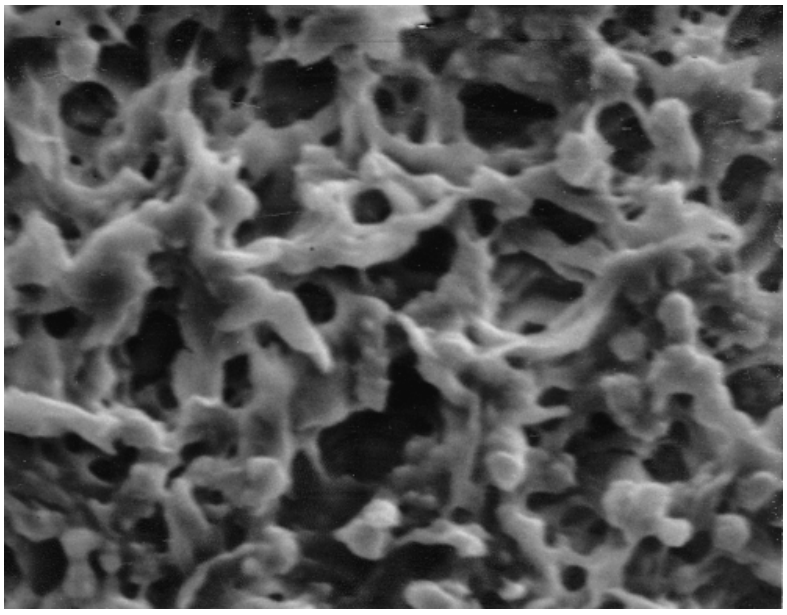

(b)

FIG. 6 Scanning electron micrographs of the surface of a clean (a) 0.2 μm Anopore membrane and (b) 0.2 μm PVDF membrane.

membrane surface. Chemical interactions involved in protein fouling are absent due to the blockage of the free cysteine residue. The cys-BSA was dissolved in a phosphate-buffered saline solution (PBS) consisting of 0.03 M KH_2PO_4, 0.03 M $Na_2HPO_4 \cdot 7H_2O$, and 0.03 M NaOH (Sigma Chemical Co., St. Louis, MO). All PBS solutions were prefiltered through 0.2-μm pore size Gelman Supor-200 membranes (Gelman Science Inc., Ann Arbor, MI) to re-

move large particulates prior to use. Protein solutions were freshly prepared before each experiment and used within 8 hours of preparation.

All filtration experiments were performed in a 25-mm diameter stirred ultrafiltration cell (Model 8010, Amicon Co., Beverly, MA) connected to an air-pressurized acrylic solution reservoir. Membranes were placed in the base of the stirred cell on top of a macroporous polyester drain disk (Osmonics, Livermore, CA) to minimize pore blockage by the support plate. The stirred cell and solution reservoir were initially filled with PBS. The membranes were flushed with a minimum of 40 mL of PBS to remove any storage or wetting agents. The PBS flow rate was then measured by timed collection using a digital balance (Sartorious Model 1580, Edgewood, NY). The stirred cell was quickly emptied, refilled with cys-BSA solution, and attached to a fresh reservoir containing additional cys-BSA solution. The system was then repressurized (within 1 minute) and the filtrate flow rate measured as a function of time. Additional details on the experimental procedures are available in Ho and Zydney (13).

EXPERIMENTAL RESULTS AND MODEL COMPARISON

The effects of pore connectivity and membrane thickness on the flux decline were examined using an Anopore membrane, a single PVDF membrane, and a series combination of 2 PVDF membranes in a sandwich arrangement. In each case the water flux was set at $2.2 \pm 0.1 \times 10^{-4}$ m/s by adjusting the transmembrane pressure drop (2.0 psi for the Anopore, 2.0 psi for the PVDF, and 4.0 psi for the 2 PVDF sandwich). The water reservoir was then rapidly replaced with a 4 g/L solution of cys-BSA with the pressure maintained at the same value used for the water flux. The initial flux during the protein microfiltration was essentially equal to the steady-state water flux evaluated immediately prior to switching to the cys-BSA solution. The data for the normalized flux as a function of filtration time are shown in the top panel of Fig. 7. The rate of flux decline was most rapid for the Anopore membrane with $J/J_0 = 0.22$ after only 50 minutes of filtration compared to $J/J_0 = 0.62$ for the PVDF membrane and $J/J_0 = 0.85$ for the 2 PVDF membrane sandwich. Scanning electron micrographs and hydraulic permeability measurements obtained with the individual PVDF membranes, separated from the two membrane stack after completion of the filtration experiment, demonstrated that the fouling occurred entirely on the upper surface of the top PVDF membrane.

Previous studies of protein fouling have demonstrated that cys-BSA fouling occurs by physical deposition of relatively large (approximately 0.6 μm diameter) protein aggregates on the upper surface of the microfiltration membrane (16). The rate of pore blockage in this system should thus be directly

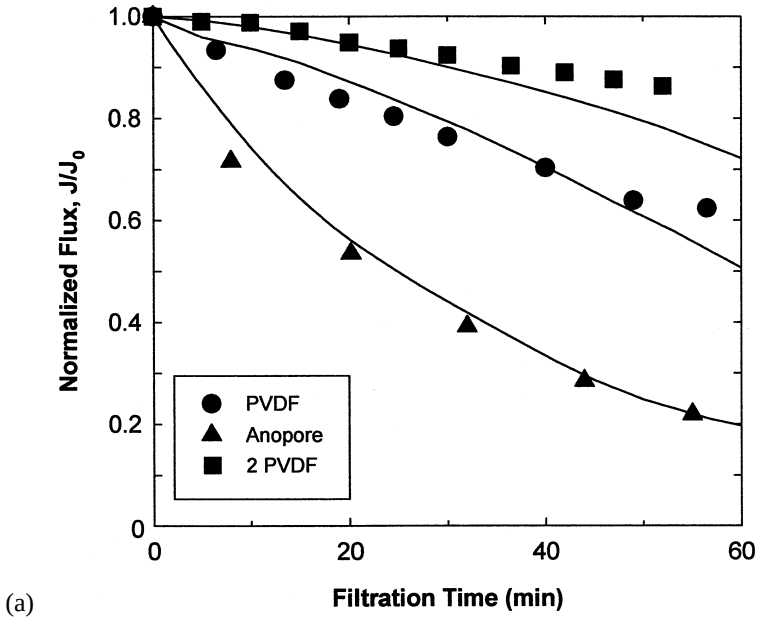

(a)

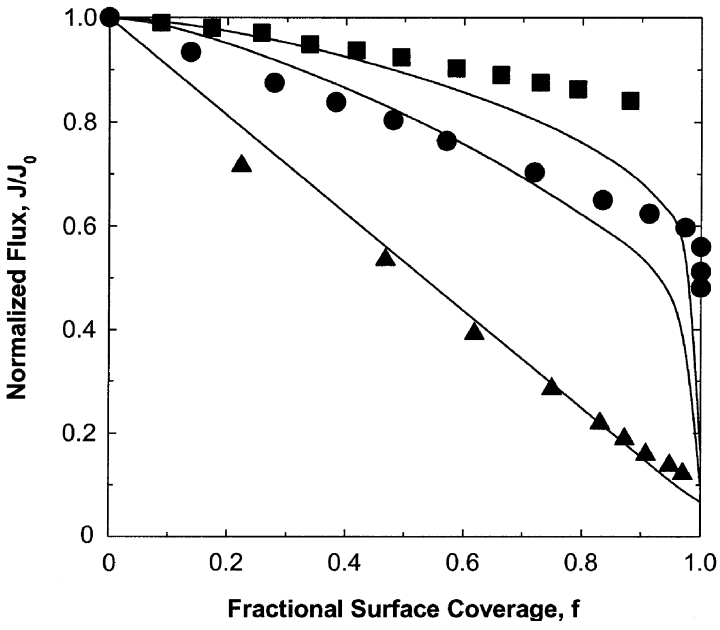

(b)

FIG. 7 Normalized filtrate flux as a function of filtration time (top panel) and fractional surface coverage (bottom panel) for the filtration of 4 g/L BSA solutions through a 0.2-μm Anopore, a 0.2-μm PVDF, and a stack of 2 PVDF membranes in series.

proportional to the mass flux of protein aggregates toward the open (uncovered) region of the membrane surface:

$$dA/dt = -\alpha_1 J_{open} A_0 C_b \tag{16}$$

where A is the area of the unblocked membrane surface, A_0 is the area of the

clean membrane, J_{open} is the filtrate flux through the uncovered area, C_b is the bulk protein concentration, and α_1 is the pore blockage parameter which is equal to the membrane area covered per unit mass of filtrate. Equation (16) can be directly integrated for a membrane with straight-through (noninterconnected) pores since J_{open} is directly proportional to the unblocked area (A) under these conditions. The final result is (6, 13):

$$J_{open}/J_0 = \exp(-\alpha_1 J_0 C_b t) \tag{17}$$

Equation (17) is equivalent to the classical pore blockage model with $J_{open} = J$. For a membrane with an interconnected pore structure (or with $\beta \neq 0$), it was necessary to integrate Eq. (16) numerically to evaluate the flux as a function of time. In this case the flux was evaluated from the numerical solution of the modified Laplace equation at a given pore blockage ($f = 1 - A/A_0$), with the rate of pore coverage (dA/dt) calculated from Eq. (16) using the numerical results for the filtrate flux. An Euler integration was then used to calculate the extent of pore coverage at time $t + \Delta t$. The numerical integration was typically performed using 100 time steps, with numerical convergence verified by repeating the calculations using one-half the original Δt.

The solid curve in the top panel of Fig. 7 for the Anopore membrane is the model calculation using the best fit values of $\alpha_1 = 0.34 \pm 0.02$ m^2/kg and $\beta = 0.08 \pm 0.03$ determined by minimizing the sum of the squared residuals between the model calculation and the experimental data. The error estimates are the standard deviations in the parameter values determined using the bootstrap method (17). This value of α_1 ($\alpha_1 = 0.34$ m^2/kg) was then used to analyze the experimental data for the single PVDF membrane, with the value of β determined from the Anopore results by simply accounting for the difference in clean membrane permeability and thickness to give $\beta = 0.09$. The best fit value of K was determined by minimizing the sum of the squared residuals between the model (assuming center blockage) and experimental data yielding $K = 2$. The model is in good agreement with the data, indicating that the pore connectivity in the PVDF membrane is able to explain the slower rate of flux decline seen in the top panel of Fig. 7. The solid curve for the 2 PVDF membrane combination is an actual model prediction using the previously determined values for α_1, β, and K, with both β and K corrected to account for the greater thickness of the PVDF stack (yielding $\beta = 0.18$ and $K = 0.5$). The model predictions are in good agreement with the filtrate flux data for the stacked membrane configuration. The small deviation at longer times could be due to aggregate deposition on top of regions already "blocked" by an earlier deposit (analogous to the behavior assumed in the intermediate blocking model) or to a breakdown in the physical model at high surface coverage (where the flow might be more appropriately described using the central void model).

In order to examine this behavior in more detail, the filtrate flux data have been replotted as a function of the fractional surface coverage in the bottom panel of Fig. 7. The fractional surface coverage was evaluated at each time point by numerical integration of Eq. (16) using the best fit values of α_1 for the different membranes. The fractional surface coverages at the end of the 60-minute filtrations are all very similar since the feed solutions contain the same amount of cys-BSA aggregates. However, the interconnected pore structure in the PVDF membranes causes a much smaller decline in flux than the Anopore membrane for the same extent of pore coverage. The difference in behavior seen for the single PVDF membrane and the 2 membrane stack is directly due to the reduction in the dimensionless permeability ratio (from $K = 2$ to $K = 0.5$) caused by the increase in membrane thickness as described by Eq. (11).

In order to compare the predictions of the interconnected pore model with those of the classical blockage models, the flux vs time results for the numerical solution were used to construct a plot of d^2t/dV^2 vs dt/dV as suggested by Eq. (1). The required derivatives were first expressed in terms of the filtrate flux:

$$\frac{dt}{dV} = \frac{1}{JA_0} \tag{18}$$

$$\frac{d^2t}{dV^2} = -\frac{1}{J^3A_0^2}\frac{dJ}{dt} \tag{19}$$

with dJ/dt evaluated by numerically differentiating the J vs t results using IMSL routine DCSDER which fits piecewise polynomials of order 4 through the "data" points. Results are shown in Fig. 8 for both the centered blockage (top panel) and centered void (bottom panel) configurations for $K = 1$, 10, and 1000. In each case the rate of pore blockage was evaluated using Eq. (16) with $\alpha_1 = 0.34\ m^2/kg$ (as determined from the cys-BSA data), $\beta = 0$, and $J_0 = 2.2 \times 10^{-4}$ m/s. Also shown for comparison are the calculated values for the Anopore and PVDF membranes determined by numerical differentiation of the data in Fig. 7 (again using Eqs. 18 and 19). The model results for $K = 1000$ (dashed curves) yield a linear relationship with slope equal to 2 which is simply the behavior predicted by the classical complete pore blocking model. The results for the membranes with more interconnected pore structures ($K = 1$ and 10) are markedly different. The initial rate of flux decline (proportional to d^2t/dV^2) is considerably smaller when $K = 1$ and 10 than that for the membrane with essentially straight-through pores ($K = 1000$) since the fluid flow is able to pass under and around the pore blockage through the interconnected pores. This effect is greater for the centered void configuration, which is consistent with the results presented in Fig. 3. As the membrane surface becomes more heavily fouled, the rate of flux decline increases sharply, with a slope greater than $n = 2$ even at large dt/dV. This effect is more pronounced for the

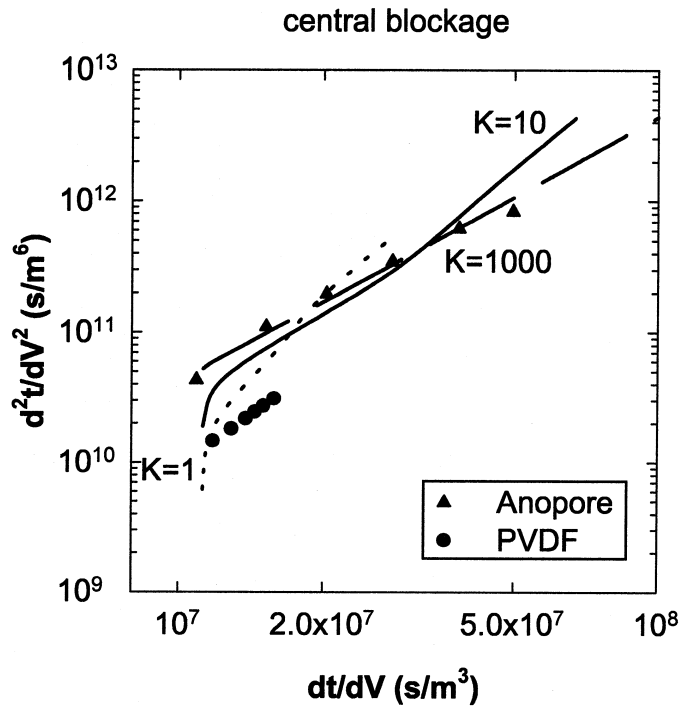

(a)

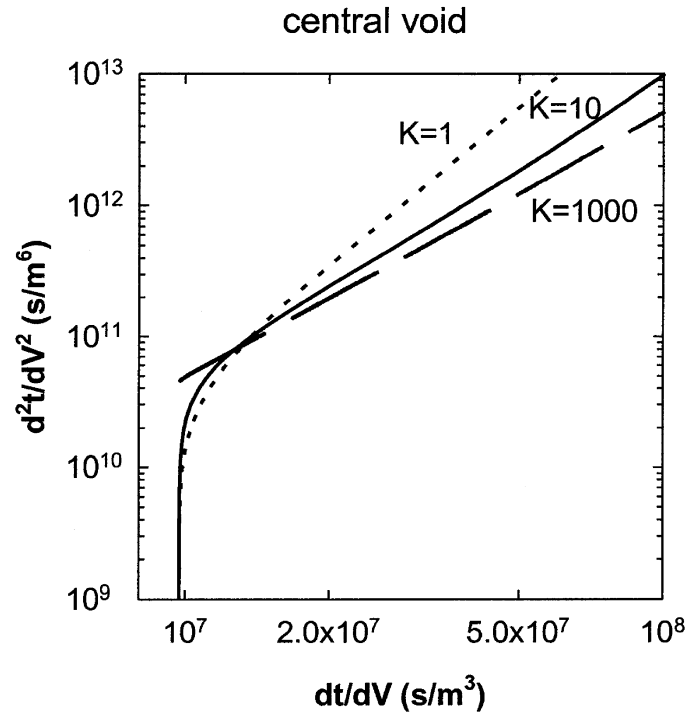

(b)

FIG. 8 Model calculations for d^2t/dV^2 as a function of dt/dV for membranes with different K values assuming no foulant superposition for (a) central blockage and (b) central void models. Solid symbols are the experimental results determined from the flux data in Fig. 7.

MARCEL DEKKER, INC.
270 Madison Avenue, New York, New York 10016

centered blockage configuration since the inwardly directed radial flow is able to penetrate all the way under the blockage even when the surface is almost completely covered. The filtrate flux results for the centered blockage configuration could not be accurately differentiated to evaluate d^2t/dV^2 at the largest dt/dV (i.e., at small J) since the normalized flux remained greater than 0.35 even when $f = 0.999$ for the membrane with the most highly interconnected pore structure ($K = 1$).

The experimental data for the Anopore membrane are in good agreement with the model calculations for $K = 1000$, consistent with the straight-through pores in the Anopore membrane. The data for the PVDF membrane are quite linear with a slope of 2.5 ($r^2 > 0.99$), which is qualitatively similar to the behavior predicted for a membrane with interconnected pores (e.g., for $K = 10$). The absence of any sharp increase in d^2t/dV^2 at small dt/dV is due to the lack of experimental data at very short times. The deviation between the model and data for the PVDF membrane is due at least in part to the flow through the blocked pores (i.e., $\beta \neq 0$), in addition to the inherent errors in evaluating d^2t/dV^2 from the numerical differentiation of the filtrate flux data.

Figure 9 shows the corresponding model calculations for a system in which the particles are allowed to settle on top of other particles on the membrane. In this case the rate of surface coverage is proportional to the fractional area remaining uncovered (A/A_0):

$$\frac{dA}{dt} = -\alpha_1 J_{\text{open}} A_0 C_b \left(\frac{A}{A_0}\right) \tag{20}$$

The results for $K = 1000$ again yield a linear relationship, but in this case the slope is equal to 1 since the governing equations reduce to the intermediate pore blocking model under these conditions (6). The initial rate of flux decline for the membranes with $K = 1$ and 10 is again considerably smaller than that for the membrane with straight-through pores ($K = 1000$). The results for the centered void configuration rapidly attain a constant slope with $n \approx 1$; however, the rate of flux decline is considerably smaller at $K = 1$ and 10 due to the smaller fractional open area (A/A_0 in Eq. 20) at a given filtrate flux (i.e., at a given dt/dV). In contrast, the rate of flux decline for the centered blockage configuration becomes nearly independent of dt/dV (i.e., $n \approx 0$) for both $K = 1$ and 10. In this case the rate of flux decline remains quite low even at very high surface coverage because the fractional area term (A/A_0) at a given J/J_0 is extremely small for the centered blockage configuration (Fig. 3).

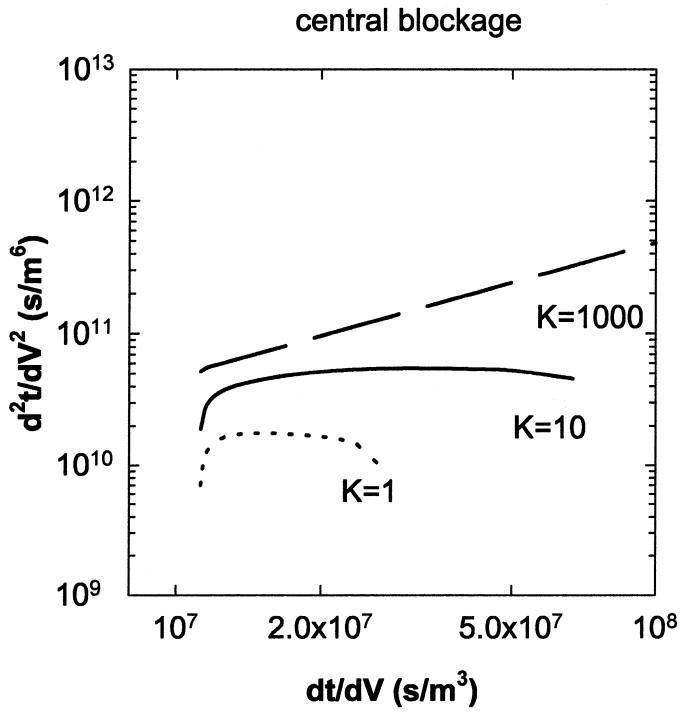

(a)

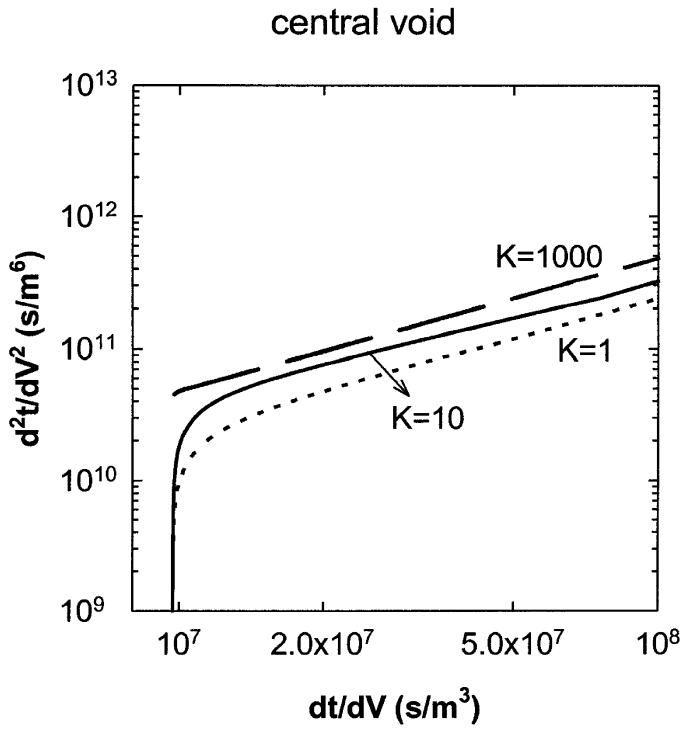

(b)

FIG. 9 Model calculations for d^2t/dV^2 as a function of dt/dV for membranes with different K values allowing for foulant superposition (Eq. 20) for (a) central blockage and (b) central void models.

MARCEL DEKKER, INC.
270 Madison Avenue, New York, New York 10016

CONCLUSION

This article provides the first detailed theoretical analysis of the velocity and pressure distributions in partially fouled membranes having interconnected pore structures. The fluid flow in these membranes was described by Darcy's law, with different values for the Darcy permeability used in the radial and transverse directions to account for the different degrees of pore connectivity. The model calculations clearly show how the fluid is able to flow radially under and around a pore blockage on the membrane surface, significantly reducing the overall hydraulic resistance to flow provided by the partially fouled membrane compared to that for a membrane with straight-through pores. The net result is that membranes with a highly interconnected pore structure are predicted to have a much slower rate of flux decline, in good agreement with previous experimental results for protein fouling of membranes with different pore morphologies (8, 13).

The rate of flux decline for membranes with an interconnected pore structure can also display a very different time dependence than that given by the classical blocking laws (which implicitly assume that the membrane has straight-through pores). For example, the calculations using the central blockage model and allowing for particle superposition (top panel in Fig. 9) yielded an exponent of $n \approx 0$ in the plot of d^2t/dV^2 vs dt/dV for membranes having an interconnected pore structure ($K = 1$ or 10) compared to $n = 1$ for a membrane with straight-through pores. In this case, experimental data for the rate of flux decline could easily be misinterpreted as indicating that fouling occurs by a cake formation mechanism (which has $n = 0$ in the classical analysis given by Eq. 1) instead of by surface pore blockage as was actually the case. Thus, considerable care must be taken in using the classical blocking laws to analyze experimental data, or identify the fouling mechanism (pore blockage, pore constriction, or cake formation), for membranes having interconnected pore morphologies.

The nondimensional form of the continuity equation (Eq. 10) shows that the effect of pore connectivity on the fluid flow, and thus the rate of flux decline, is determined by the magnitude of the dimensionless permeability ratio, K. It is important to recognize that K is not only a function of the radial and transverse permeabilities (K_r/K_z), but is also proportional to $(r_{blockage}/\delta_m)^2$. Thus, the rate of flux decline decreases with increasing membrane thickness since the pore blockage disturbs the flow over a smaller fractional depth into the thicker membrane (as described by the reduction in K with increasing δ_m). This result is in good agreement with the experimental data in Fig. 7 which show a much slower rate of flux decline for the 2-membrane stack compared to the single PVDF membrane. In addition, the model would suggest that a very thin membrane will behave as if it has straight-through pores even if the membrane itself

is isotropic (i.e., $K_r = K_z$) due to the very small value of K. This effect was observed by Ho and Zydney (13) in their analysis of protein fouling through asymmetric polyethersulfone membranes having a very thin (approximately 0.5 μm thick) skin layer. These results indicate that it should be possible to develop membranes with improved fouling characteristics by proper design of the membrane pore morphology (e.g., the pore connectivity or overall membrane thickness), an approach which has been largely neglected in both academic and commercial efforts to develop low-fouling membranes.

NOTATION

A	area of unblocked membrane (m^2)
A_0	area of the clean membrane (m^2)
C_b	bulk protein concentration (g/L)
f	fractional pore blockage
J	filtrate flux (m/s)
J_0	initial filtrate flux (m/s)
J_{open}	flux through uncovered membrane surface (m/s)
K	permeability ratio ($K_z r^2_{blockage}/K_r \delta^2_m$)
K_r	Darcy permeability in radial direction ($m^3 \cdot s/kg$)
K_z	Darcy permeability in axial direction ($m^3 \cdot s/kg$)
L_p	hydraulic permeability of the fouling layer ($m^2 \cdot s/kg$)
P_{feed}	feed stream pressure (N/m^2)
$P_{filtrate}$	filtrate pressure (N/m^2)
$r_{blockage}$	radius of the blockage (left panel in Fig. 1) (m)
$r_{cylinder}$	radius of the flow cylinder (m)
r_{open}	radius of the unblocked region (right panel in Fig. 1) (m)
t	filtration time (s)
V	total collected filtrate volume (m^3)
V_r	radial velocity (m/s)
V_z	axial velocity (m/s)
Y	dimensionless axial coordinate (z/δ_m)

Greek Letters

α_1	pore blockage parameter (m^2/kg)
β	dimensionless fouling layer permeability ($\delta_m L_p/K_z$)
ρ	dimensionless radial coordinate ($r/r_{blockage}$ or r/r_{open})
θ	dimensionless pressure [$(P - P_{feed})/(P_{filtrate} - P_{feed})$]
ψ	stream function (m^3/s)
ε	membrane porosity
δ_m	membrane thickness (m)

MARCEL DEKKER, INC.
270 Madison Avenue, New York, New York 10016

ACKNOWLEDGMENT

This work was supported in part by a grant from the National Science Foundation.

REFERENCES

1. P. C. Carman, "Fundamental Principles of Industrial Filtration," *Trans. Inst. Chem. Eng. (London), 16*, 168 (1938).
2. P. H. Hermans and H. L. Bredée, "Zur Kenntnis der Filtrationsgesetze," *Rec. Trav. Chim. Pays-Bas, 54*, 680 (1935).
3. P. H. Hermans and H. L. Bredée, "Principles of the Mathematical Treatment of Constant-Pressure Filtration," *J. Soc. Chem. Ind., 55T*, 1 (1936).
4. V. E. Gonsalves, "A Critical Investigation on the Viscose Filtration Process," *Rec. Trav. Chim. Pays-Bas, 69*, 873 (1950).
5. H. P. Grace, "Structure and Performance of Filter Media," *AIChE J., 2*, 307 (1956).
6. J. Hermia, "Constant Pressure Blocking Filtration Laws: Application to Power Law Non-Newtonian Fluids," *Trans. Inst. Chem. Eng., 60*, 183 (1982).
7. C. Visvanathan and R. Ben Aïm, "Studies on Colloidal Membrane Fouling Mechanisms in Crossflow Microfiltration," *J. Membr. Sci., 45*, 3 (1989).
8. W. R. Bowen and Q. Gan, "Properties of Microfiltration Membranes: Flux Loss during Constant Pressure Permeation of Bovine Serum Albumin," *Biotechnol. Bioeng., 38*, 688 (1991).
9. M. Hlavacek and F. Bouchet, "Constant Flow Rate Blocking Laws and an Example of Their Application to Dead-End Microfiltration of Protein Solutions," *J. Membr. Sci., 82*, 285 (1993).
10. E. M. Tracey and R. H. Davis, "BSA Fouling of Track-Etched Polycarbonate Microfiltration Membranes," *J. Colloid Interface Sci., 167*, 104 (1994).
11. S. T. Kelly and A. L. Zydney, "Mechanisms for BSA Fouling during Microfiltration," *J. Membr. Sci., 107*, 115 (1995).
12. S. T. Kelly, W. S. Opong, and A. L. Zydney, "The Influence of Protein Aggregates on the Fouling of Microfiltration Membranes during Stirred Cell Filtration," *Ibid., 80*, 175 (1993).
13. C. C. Ho and A. L. Zydney, "Effect of Membrane Morphology on the Initial Rate of Protein Fouling during Microfiltration," *Ibid., 155*, 261 (1999).
14. A. Krogh, "The Supply of Oxygen to the Tissues and the Regulation of the Capillary Circulation," *J. Physiol. 52*, 457 (1918).
15. L. J. Kelsey, M. R. Pillarella, and A. L. Zydney, "Theoretical Analysis of Convective Flow Profiles in a Hollow-Fiber Membrane Bioreactor," *Chem. Eng. Sci. 45*, 3211 (1990).
16. S. T. Kelly and A. L. Zydney, "Effects of Intermolecular Thiol–Disulfide Interchange Reactions on BSA Fouling during Microfiltration," *Biotechnol. Bioeng., 44*, 972 (1994).
17. P. J. Huber, *Robust Statistics*, Wiley, New York, NY, 1981.

Received by editor December 7, 1998
Revision received February 1999

Request Permission or Order Reprints Instantly!